Effect of low-intensity whole-body vibration on bone defect repair and associated vascularization in mice

Takeshi Matsumoto[1,2], Daichi Goto[2]

[1]*Department of Mechanical Science, Tokushima University Graduate School of Science and Technology, 2-1 Minamijosanjima, Tokushima 770-8506, Japan*

[2]*Department of Mechanical Science and Bioengineering, Osaka University Graduate School of Engineering Science, 1-3 Machikaneyama, Toyonaka 560-8531, Japan*

Corresponding author: Takeshi Matsumoto, PhD

Tokushima University Graduate School of Science and Technology

2-1 Minamijyousanjima, Tokushima 770-8506, Japan

t.matsumoto@tokushima-u.ac.jp

Total number of words: 7163

Number of words of the abstract: 215

Number of figures: 5

Number of tables: 1

Abstract

Low-intensity whole-body vibration (LIWBV) may stimulate bone healing, but the involvement of vascular ingrowth, which is essential for bone regeneration, has not been well examined. We thus investigated the LIWBV effect on vascularization during early-stage bone healing. Mice aged 13 weeks were subjected to cortical drilling on tibial bone. Two days after surgery (day 0), mice were exposed daily to sine-wave LIWBV at 30 Hz and 0.1 g peak-to-peak acceleration for 20 min/day (Vib) or were sham-treated (sham). Following vascular casting with a zirconium-based contrast agent on days 6, 9, or 12 and sacrifice, vascular and bone images were obtained by K-edge subtraction micro-CT using synchrotron lights. Bone regeneration advanced more in the Vib group from days 9 to 12. The vascular volume fraction decreased from days 6 to 9 in both groups; however, from days 9 to 12, it was increased in shams, while it stabilized in the Vib group. The vascular volume fraction tended to be or was smaller in the Vib group on days 6 and 12. The vessel number density was higher on day 9 but lower on day 12 in the Vib group. These results suggest that the LIWBV-promoted bone repair is associated with the modulation of vascularization, but additional studies are needed to determine the causality of this association.

Keywords: low-magnitude vibration, cortical bone defect, vascular ingrowth, synchrotron radiation, K-edge subtraction

Author biography

Takeshi Matsumoto received Ph.D. degree in Engineering from Nagoya University in 1992 and is currently a Professor of Biomedical Engineering in Tokushima University Graduate School of Science and Technology. His research interest is bone microcirculation.

Daichi Goto completed his Master's degree at Osaka University in 2012. He is currently working as an engineer for mechanical designs at Mitsubishi Electric Corporation since 2013.

1. Introduction

Prolonged bed rest or physical immobility following bone fractures, especially hip fractures in older people, may induce deconditioning and motor deterioration. This could lead to severe secondary complications that require nursing care or even lead to in-hospital death [18, 23, 26]. Therefore, shortening the duration of bed rest by accelerating healing of fractures and allowing for early rehabilitation or partial weight-bearing are clinically important [61]. Bone regenerative capacity is mechanical stimulus-dependent and moderate loading accelerates healing of fractures [3, 54]. Therefore, mechanical stimuli, if available soon after treatment for fractures, will accelerate healing of fractures towards early achievement of structural resistance needed for undergoing rehabilitation.

Potential mechanical stimuli available during the early stage of healing of fractures may be provided by low-intensity whole-body vibration (LIWBV). LIWBV delivers mechanical stimuli to the appendicular and axial skeleton via a high-frequency and low-magnitude vibrational platform [40, 49]. Compared with loading modalities that induce large-magnitude mechanical signals, a low intensity ($< 1 \times$ g in general; g = 9.81 m/s^2) of LIWBV enables it to be more accessible for patients with fractures at a stage prior to rehabilitation. The benefits of LIWBV have been reported in fracture healing in rodent models [29, 43, 53, 56].

Vascular ingrowth, which is an essential process for inducing bone regeneration during healing of fractures [7, 52, 55], is involved in LIWBV-stimulated healing of fractures. Hypoxia due to vascular disruption accompanying bone injury stimulates production of angiogenic factors, such as vascular endothelial growth factors, by promoting accumulation of hypoxia-inducible factors [27, 50]. This pathway is a critical mediator of angiogenesis and is modulated by mechanical stimuli. Unloading-induced retardation of healing of fractures is associated with decreased angiogenesis [2, 35, 37, 59], whereas mechanical stimuli can enhance angiogenesis along with osteogenesis for bone regeneration [4, 19, 39].

The pro-angiogenic response to LIWBV has been reported in a rat femoral closed fracture model [8]. However, detailed data on vascularization relevant to LIWBV-stimulated healing of fractures are still lacking. To address this gap in knowledge, we evaluated the involvement of vascularization in LIWBV-enhanced bone regeneration during early-stage healing in mice. Using a zirconium-based contrast agent (ZrCA) for vascular casting [33] and its K-edge absorption spectra, three-dimensional images of vasculature and newly formed bone were acquired by synchrotron radiation-based subtraction micro-CT (SRSμCT).

2. Methods

Experiments were conducted in accordance with the guiding principles of the American Physiological Society and with the approval of the Animal Research Committee of Osaka University Graduate School of Engineering Science. Details on ZrCA and SRSμCT have been described elsewhere [33].

2.1 General procedures

Forty-eight, 13-week-old, male C57BL/6 mice (Clea Japan, Tokyo, Japan), which is an inbred strain exhibiting highly mechanosensitive bones [25, 48], were anaesthetized with isoflurane. The skin over the medial aspect of the right lower leg was shaved, swabbed with povidone iodine, and incised. A full-thickness unicortical hole was created approximately 3 mm proximal to the tibio-fibula junction using a 0.5-mm diameter drill rotating at 11,000 rpm (Muromachi Kikai, Kyoto, Japan). Drill margins were frequently irrigated with saline to avoid thermal necrosis, and the drill hole was rinsed with a flushing syringe to discard bone fragments. After arrest of bleeding from the bone marrow, the skin was sutured and swabbed again. All mice were singly housed in a plastic cage under controlled conditions (12-h light/dark cycle, 25°C, 60% humidity) and allowed free access to a standard diet (CE-2; Clea Japan) and tap water.

On the second day following drill-hole surgery (day 0), the mice were randomly divided into two groups (n = 24 each) as follows: treated with LIWBV (Vib) and sham-treated (sham). Mice in the Vib group were exposed daily to 20 min of vertical LIWBV (sine wave, 30 Hz, 0.1 g peak-to-peak). Six mice at a time were placed in a compartmented cage that was firmly screw-fixed to a rigid vibration platform. The platform was driven by an electromagnetic actuator connected to a power supply/amplifier/controller (Big-Wave; Asahi Seisakujo, Tokyo, Japan). Using data received from an accelerometer (P51SC; Fuji Ceramics, Tokyo, Japan) attached to the platform, the vibration controller generated the input signal, which controlled the gain of the amplifier to produce the required sine-wave vibration. Mice in the sham group were treated similarly, but in a non-operated state. The interventions were commenced and introduced daily thereafter at the same time until sacrifice.

On post-surgery days 6, 9, and 12, the animals were sacrificed for sample preparation. These time points were chosen on the basis of conventional in vivo CT scans of mouse femora subjected to 0.8-mm drill-hole surgery, showing that newly formed bone appeared in the defect a week after the surgery and

woven bone bridged almost the entire defect after another week [22]. On each day of observation, eight mice per group were laparotomized under general anaesthesia, and the abdominal artery and vein distal to the renal branches were exposed by blunt dissection. The body was kept warm using an infrared heater (HIR-227; Omron, Kyoto, Japan) and the gut was moistened with warmed saline as needed. Following intravenous heparin injection (1000 U), mice were euthanized by an intraperitoneal overdose of pentobarbital sodium, and the chest was rapidly opened by median thoracotomy. A 22 G polyethylene catheter was inserted into the left ventricle through the apex, and the right atrium was cut open to allow fluid to exit.

The vascular network was flushed with 50 mL of heparinized saline (37°C, 100 U/ml) and then with 5 mL of 0.1 M phosphate buffer (37°C). This flushing was followed by gravity-feed perfusion at 120 mmHg with ZrCA (40°C). This contrast agent is a 1.2-μm-filtered mixture of 30 mL of 1.2% w/v agarose (Super LM; Nacalai Tesque, Kyoto, Japan) in 0.1 M phosphate buffer and 15 mL of a 62% w/v water-based suspension of colloidal zirconium dioxide particles of 0.07–0.1 μm (ZR40BL; Nissan Chemical Industries, Tokyo, Japan). The phosphate buffer infusion prior to ZrCA perfusion was required to avoid any adverse effects of saline on ZrCA. The side of the hindlimb with the defect was moved occasionally by hand to facilitate extensive perfusion. The end point of vascular filling with ZrCA was determined by the appearance of superficial vessels in the femoral musculature and purity of the outflow. Once perfusion was completed, the abdominal artery and vein were ligated, and the entire body was immersed in an ice-cold water bath for approximately 1 h and stored overnight at 4°C. The right tibia was harvested, dissected free of soft tissue, and soaked in 4% paraformaldehyde until analysis.

2.2 Synchrotron radiation-based subtraction micro-CT

Each specimen was sealed in polyethylene tubes containing 4% paraformaldehyde and scanned by high-resolution computed tomography (CT) (SPring-8, Harima, Japan) using monochromatic synchrotron lights just above (18.1 keV) and below (17.9 keV) the K-absorption edge of ZrCA. A digital CMOS camera (C11440-22CU; Hamamatsu Photonics, Hamamatsu, Japan) equipped with a 10-μm-thick phosphor screen ($Gd_2O_2S:Tb^+$) and a beam monitor (BM2: f = 35 mm) was used to detect the transmitted synchrotron light. Scanning was performed over an angular range of 0–180° at 0.1° with a 0.2-s exposure per frame. For calibration to compensate for X-ray source instability, 30 images of the X-ray beam alone were recorded at

the start and end of each scan. For background correction, 30 dark images were also collected. Each scan dataset was reconstructed with a two-dimensional filtered backward projection algorithm using custom-built software. This algorithm providing contiguous two-dimensional images composed of 2.76-μm cubic voxels with 8-bit grey-scale resolution (0 [black] to 255 [white]).

Image subtraction between 18.1- and 17.9-keV image stacks allowed selective visualization of vascular structures owing to the sharp K-edge absorption jump in ZrCA in 18.1-keV scanning. Prior to image subtraction for extraction of the vascular region, every image was redigitized such that the voxel value of the linear absorption coefficient, μ (/cm), was calculated by 0.392 × grey value. Pairs of 18.1- and 17.9-keV image stacks were then corrected for misalignment by mutual information-based image registration [32]. In this process, the 18.1-keV (floating) image stack was aligned with the 17.9-keV (reference) image stack. Bone regions in the 17.9-keV image stack were then expanded by three-dimensional maximum filtering. This was performed to reduce unwanted residuals near bone boundaries in the subtracted image owing to the partial-volume effect. Finally, the 17.9-keV image stack was subtracted from the 18.1-keV image stack. The subtracted image stack was filtered with 3 × 3 × 3 voxel averaging and the vascular region was segmented from the rest using minimum cross-entropy thresholding [45].

For quantitative evaluation of hydroxyapatite density (d.Hap, mg/cm^3), 17.9-keV images of capillary tubes containing K_2HPO_4 solution at various concentrations, serving as hydroxyapatite phantoms, were acquired in the same manner as imaging specimen. Phantom images were redigitized such that μ was calculated by 0.0588 × grey value, leading to the relation: d.HAp = 8.18 × grey value − 156 ($r^2 > 0.999$). The original 17.9-keV image stacks were similarly redigitized and filtered by 3 × 3 × 3 voxel averaging. All regions of $\mu \geq 4.72$/cm (i.e., d.HAp ≥ 500 mg/cm^3), except the vascular regions, were classified as regenerated bone. ImageJ 1.46k software with a custom C program was used for image processing. Figure 1 shows radiographs (Figure 1A, B) and reconstructed three-dimensional images (Figure 1C, D) of a representative tibial bone defect acquired by 17.9- and 18.1-keV scanning and the extracted images of bone and vascular structures within the defect (Figure 1E, F).

Fig. 1 →

2.3 Quantitative parameters for vascular and bone structures

For structural analysis, a cylindrical region of interest (diameter, 470 μm; height, 110 μm) was chosen centrally within the cortical defect. These sizes were close to but sufficiently below the initial drill-hole diameter and the thickness of a nearby intact cortical bone, respectively. The vascular volume fraction (V.Vf, %) vessel thickness (V.Th, μm), the number density of node-to-node or node-to-free-end vessel segments (V.N, /mm^3), bone volume fraction (B.Vf, %), bone thickness (B.Th, μm), and bone spacing (thickness of the background) (B.Sep, μm) were calculated. Bone structural indices were calculated for specimens on days 9 and 12, but not on day 6, because bone regeneration was barely detectable at this healing stage. The BoneJ plugin 1.3.5 for ImageJ 1.46k [11] was used to determine all indices, except for V.Th. For determining V.Th, the local vessel thickness was defined as the thickness of the largest sphere falling inside the vascular space with its centre on a vascular skeleton line provided by a thinning algorithm V.Th was defined as an average of these thicknesses over all skeleton lines. The thickness of each vessel segment was also determined as an average of local vessel thicknesses over its skeleton line, and vessel size-specific V.N was calculated. Using the μ-d.HAp relation, local d.HAp values were determined for newly formed bone on days 9 and 12.

2.4 Tibial bone strain measurement

Using three additional male C57BL/6 mice aged 12 weeks and weighing 25-26 g, mechanical strain on the tibial diaphyseal surface was measured in the longitudinal bone direction under LIWBV loading. Under anaesthesia with pentobarbital sodium (40 mg/kg, i.p.), the skin over the medial aspect of the right lower leg was shaved, swabbed with 2% lidocaine jelly, and incised. The antero-medial surface of the tibial diaphysis was scraped with a cotton bud, and a miniature uniaxial strain gauge (KFR-02N-120-C1-11; Kyowa Electronic Instruments, Tokyo, Japan) was glued with α-cyanoacrylate monomer to the surface. Mice were placed so that they were standing on the vibrating plate during recovery from anaesthesia. The output signal from the strain gauge was recorded over several seconds under LIWBV and sham-LIWBV loading at a sampling rate of 1 kHz with a sensor interface (PCD-300A; Kyowa Electronic Instruments) and software (PCD-30A; Kyowa Electronic Instruments). After 28–32 Hz band-pass filtering, the mean difference between consecutive bottom-top peaks of strain was calculated as an index of magnitude of the strain signal.

2.5 Statistical analysis

The data are expressed as means ± SEM unless otherwise indicated. The Kolmogorov–Smirnov test was performed to test for normal distribution of values. Non-parametric statistical analysis was performed because not all experimental groups were normally distributed. The two-tailed Mann–Whitney U test was used to examine statistical significance between the sham and Vib groups, and between bone structural indices on days 9 and 12 in each group. The Kruskal–Wallis test followed by Dunn's post hoc test were used to examine statistical significance between vascular structural indices on days 6, 9, and 12 in each group. All data were analysed by Prism 6 (GraphPad Software; San Diego, CA). $P < 0.05$ was considered statistically significant.

3. Results

Body weight (mean ± SD) in the sham and Vib groups was 26.9 ± 0.3 and 27.1 ± 0.2 g on day 0, 28.0 ± 0.7 and 28.7 ± 0.9 g on day 6, 28.8 ± 1.3 and 28.3 ± 0.7 g on day 9, and 29.7 ± 0.9 and 30.0 ± 1.4 g, respectively, on day 12. Body weight did not significantly change over time or between groups.

Representative three-dimensional reconstruction within the bone defect is shown for each group in Figure 2. The structural indices on bone and vasculature are shown in Table 1. On day 6, only vascular ingrowth was observed. No differences were found in V.Vf and V.N between the Vib and sham groups. However, V.Th was smaller in the Vib group than in shams, which contributed to a tendency for a smaller V.Vf in the Vib group ($P = 0.073$). On day 9, bone regeneration with reduced vascularity was observed in both groups, filling the defect at a higher fraction with woven-like bone than with blood vessels (B.Vf > V.Vf). At this stage, every bone index was similar between the Vib and sham groups. From days 6 to 9, V.Th and V.N decreased, but this was significant only in shams. Accordingly, V.Vf decreased to a smaller extent in the Vib group than in shams, resulting in similar V.Th and V.Vf between the groups, and a significantly larger V.N in the Vib group on day 9. On day 12, bone regeneration advanced to a higher extent in the Vib group, and B.Vf and B.Th were significantly higher and B.Sep was significantly lower in the Vib group than in shams. Vascularization showed a different trend between the Vib and sham groups from days 9 to 12. In shams, V.Vf, V.Th, and V.N were increased, whereas in the Vib group, V.Vf and V.Th underwent little change, and V.N was significantly decreased. This resulted in a significantly smaller V.Vf and V.N, and a tendency for a smaller V.Th ($P = 0.053$) in the Vib group than in shams on day 12.

Fig. 2 →

Table 1 →

Figure 3 shows vessel size-specific V.N for seven thickness ranges. On day 6, both groups showed similar distribution of peak V.N in the thickness range of 8–16 μm. However, at this time, V.N was smaller in the range of 24–40 μm and tended to be smaller in the range of > 48 μm (P = 0.081) in the Vib group than in shams. On day 9, angiogenic vessels were distributed mostly in the range of < 16 μm in both groups. There was a trend toward a higher V.N in the Vib group than in shams in the capillary size range of < 8 μm (P = 0.065), contributing to an overall higher V.N in the Vib group. On day 12, V.N in the Vib group was significantly smaller in the range of 8–32 μm, and tended to be smaller in the ranges of 32–40 μm (P = 0.095) and > 48 μm (P = 0.061) than those in shams.

Fig. 3 →

The relative distribution of bone volume versus d.HAp within the defects on days 9 and 12 is shown in Figure 4. No difference was found in d.HAp distribution on day 9 between the Vib and sham groups. From days 9 to 12, the distribution of d.HAp shifted to the right in both groups. Although skewness did not differ between the two groups, the distribution peaked at a higher d.HAp in the Vib group (885 ± 8 vs. 842 ± 18 mg/cm^3, P < 0.05). This finding indicated the accelerating effect of Vib on mineralization. The mean and median d.HAp were similar between the Vib and sham groups (Vib: 798 ± 8 and 803 ± 8 mg/cm^3; sham: 775 ± 14 and 776 ± 15 mg/cm^3).

Fig. 4 →

Figure 5 shows an example of strain recordings on the tibial diaphyseal surface of the same mouse standing on the operative (Figure 5A) and non-operative (Figure 5B) vibration platform. Strain signals were consistent across mice. No distinct sinusoidal pattern in accordance with LIWBV loading was found. However, band-pass filtering between 28–32 Hz extracted sinusoidal strain oscillations induced by LIWBV. Peak-to-peak magnitudes of the band-pass filtered signals (mean ± SD) were 1.05 ± 0.14, 0.97 ± 0.07, and 0.98 ± 0.10 με for each of three mice with LIWBV loading. These values were approximately seven times higher than the magnitudes of similarly filtered signals obtained in the absence of LIWBV loading (mean: 0.14 ± 0.06 με, n = 3 mice).

Fig. 5 →

4. Discussion

Using the combined techniques of SRSμCT and ZrCA for vascular casting, we showed LIWBV-induced acceleration of bone regeneration with modulation of associated vascularization in mouse tibial drill-hole injury during the early period of healing. At the stage of vascular ingrowth before bone regeneration (day 6), LIWBV altered vascularity by reducing the amount of vessels with relatively large thickness. At the stage accompanying overall reduction in vasculature after the onset of bone regeneration (days 6–9), LIWBV resulted in a trend toward increased formation of capillary-sized vessels (≤ 8 μm thickness), but had no effect on bone regeneration. The effect of LIWBV on vascularization markedly appeared at the stage of progress in bone healing (days 9–12). LIWBV accelerated bone regeneration in terms of volume and mineral density, but reduced rather than increased vascularity, with the exception of capillary-sized vessels.

Angiogenesis is indispensable for bone regeneration, especially in the early stages of healing of fractures [21, 52]. Vascular ingrowth in the injury site encourages osteogenesis by sustaining a high metabolic activity in osteoblasts engaged in bone repair. This ingrowth also serves as a migration route for osteoprogenitors [31, 55] and as a source for bone growth factors [30, 41]. Angiogenesis is primarily affected by a low oxygenation state of fractured tissue, but is affected by mechanical conditions. Mechanical stimuli may increase production of angiogenic factors, such as vascular endothelial growth factor (VEGF), thereby enhancing vascular ingrowth [4, 19, 60]. Therefore, LIWBV might stimulate vascularization and accelerate bone repair accordingly. Indeed, a previous study demonstrated that LIWBV-stimulated bone regeneration accompanied enhancement of angiogenic activity and vascularization in normal rats or in an osteoporotic rat model of closed fracture healing [8]. However, the relation between vascularization and bone regeneration is not likely to be simple in a mouse tibial defect model, and LIWBV may have a more complicated effect on vascularization at early healing stages.

A balance between angiogenic and osteogenic activity appears to be crucial at each healing stage [15, 47]. Temporal hypoxia after bone injury recruits mesenchymal stem cells (MSCs) and progenitor cells (MPCs) to the injury site. This situation leads to differentiation of these cells toward an endothelial lineage, thereby encouraging vascular ingrowth for oxygen and nutrient supply sufficient for cell survival. MSCs and MPCs can also undergo endothelial, as well as osteoblastic, differentiation depending on mechanical stimuli [10, 36]. Bone injury with mechanical stability, as in the present defect model, provides *de novo* bone regeneration by osteoblasts (intramembranous ossification) [38]. Therefore, based on our finding of less vessel formation in the Vib group than in shams on day 6, we speculate that LIWBV leads to more

osteoblastic and less endothelial differentiation in MSCs and MPCs. This shift in cellular differentiation then facilitates the transition to the next healing stage of callus formation. An inhibitory effect of LIWBV on adipogenesis in MSCs [13] would also lead to an increase in osteoblastic differentiation. Nonetheless, a sufficient vascular supply to the injury site might have been ensured in our study because a reduction in vessel formation occurred mainly in relatively large-sized vessels. However, formation of capillary-sized vessels, which is critical for perfusion efficacy, appeared to be unaffected. A previous study showed that exogenous administration of VEGF during vasculogenesis in avian embryos led to formation of vessels with abnormally large lumens [12]. Therefore, VEGF might be intrinsically overexpressed after vascular disruption, resulting in excessive vascularization.

After entering the phase of bone regeneration, the central role of the vasculature changes to sustainment of a high metabolic demand in osteogenesis. Therefore, in our study, the tendency for increased formation of capillary-sized vessels in the Vib group on day 9 might have resulted from elevation of osteogenic activity requiring a sufficient blood supply. This increase in capillary-sized vessels might also reflect an increase in type H vessels. Type H vessels are a rich source of several growth factors that are relevant to survival and proliferation of perivascular osteoprogenitors [28]. The cumulative action of LIWBV, presumably for preferred osteoblastic differentiation, could result in enhanced bone regeneration on day 12, with reduced vascularity in a limited space, while still maintaining sufficient capillary-sized vessels. Overall, LIWBV might couple osteogenic and angiogenic activity in an efficient manner, thereby accelerating bone healing. Further studies are necessary to investigate the balance of vascularization and bone regeneration at each phase of bone healing and its modulation by LIWBV loading.

Under the present setting of LIWBV, the strain amplitude at the defect site was only 1 με. The 12-week-old mice used for the strain measurements were 1 to 3 weeks younger than the tibial defect model of mice during undergoing LIWBV. Accordingly, there are some differences in body weight and skeletal maturity, which may affect the magnitude of strain signals. However, the body weight difference is around 10%, and the skeletal tissue has already reached a high level of maturity at the age of 12 weeks. Thus, the measured strain signals would be comparable in magnitude to those induced in the tibial defect model. Vibration-induced enhancement of intramembranous bone regeneration was also observed in a cranial defect model of mice [43] and rats [24]. These mice were exposed to 30-Hz and 0.3-g LIWBV loading and rats were subjected to 45-Hz and 0.4-g vibratory head motion. Bone strain was not measured in these studies.

However, based on the finding that 45-Hz and 0.3-g vibratory motion generates approximately 1 με on a mouse tibial bone when its lower leg is at a non-weight-bearing state [16], these strain magnitudes in the cranial bone are presumed to be a maximum of a few microstrains. Therefore, even with induction of infinitesimally small deformations in bone tissue, LIWBV appears capable of accelerating intramembranous bone healing.

Cell deformation within bone tissue matrix under LIWBV loading is much lower than that normally associated with daily activities. Therefore, unless there is a strong mechanism for cellular-level strain amplification as proposed in the osteocyte process [20], LIWBV-induced cell deformation is unlikely to be a physical input beyond the threshold for cellular responsiveness. As suggested in previous studies [1, 17], out-of-phase motion of the nucleus relative to the cell body or the cell body relative to the extracellular matrix may be a mechanical input to which MSCs, MPCs, and their progeny can respond. Indeed, intracellular displacement of the nucleus could alter the force distribution in the cytoskeleton and commit to an osteogenic response [57, 58].

Although LIWBV settings that are effective for bone healing vary among studies, the relationship between osteogenic activity and vibrational magnitude of LIWBV appears to be non-monotonic [1, 9]. Additionally, the osteogenic effect of LIWBV depends on vibration frequency [46]. There may be a LIWBV setting that maximally potentiates its effect on bone regeneration. However, examination of an optimal LIWBV is beyond the scope of this study. Other than the direct action of LIWBV at a cellular level, LIWBV may influence bone regeneration via systemic modulation in growth hormonal, neuromuscular, and circulatory status [5, 42, 44, 51]. However, the anabolic response to vibratory stimuli is measurable only in the tibiae on the side of the unilateral hindlimb to which vibratory stimuli are exclusively applied [17]. This suggests that LIWBV-induced mechanical stimuli work locally to enhance bone regeneration.

There are some limitations of this study. First, the present result of enhanced bone healing and modulated vascularization is entirely due to the action of LIWBV on intramembranous ossification. Additionally, the bone injury site was directly beneath the skin, excluding bone–muscle interactions during healing [6]. Therefore, LIWBV would yield different outcomes in bone regeneration, vascularization, and their coupling during healing of more clinically relevant fractures such as femoral closed fractures [8]. In this situation, bone arises from a combination of intramembranous and endochondral ossification with involvement from muscular tissue. Second, we measured neither chemical nor mechanical properties of

newly formed bone, which are affected by LIWBV [34]. Future studies that assess the effect of LIWBV on these properties, such as bone mineral, collagen, and stiffness, as well as their relationships, will provide useful information. Third, more CT scans at different time points are required for exploring the involvement of vascularization in the LIWBV-enhanced bone defect repair. In vivo CT with suitable vascular contrast agents, which allows repetitive scanning in a single rodent, might be potentially available for multiple time-point scans, though its spatial resolution limited by radiation dose [14] will be insufficient especially for microvascular imaging. Finally, we did not measure the expression of angiogenic and osteogenic growth factors involved in bone healing. This issue should be addressed in future experiments for determining the LIWBV-induced balance shift between angiogenic and osteogenic recruitment.

In conclusion, using the combined techniques of SRSμCT and ZrCA for vascular casting, this study shows that extremely low-amplitude LIWBV enhances early-stage bone repair in mouse cortical bone with modulation of vascular ingrowth in a vessel size-dependent manner. Enhanced bone regeneration does not necessarily accompany increased development of vasculature. Instead, LIWBV reduces, rather than increases, the amount of vessels with a relatively large thickness, while maintaining or modestly increasing capillary-sized vessels. This finding indicates that stimulation of angiogenesis as a fracture treatment strategy might not consistently result in improved outcomes. Microstrain-order bone tissue strain generated under LIWBV loading suggests its therapeutic potential for bone healing under stiff fixation. Further studies are required to examine whether the effect of LIWBV can be confirmed during bone healing in the absence of weight bearing for determining its availability for patients with fractures who are confined to bed.

Acknowledgements

The authors are indebted to Shota Sato (Osaka University Graduate School of Engineering Science) for his assistance with image processing and analysis. This work was supported in part by Grants in-Aid for Scientific Research from the Ministry of Education, Culture, Sports, Science and Technology of the Japanese government (grant nos. 24650265 and 26282120). The synchrotron radiation experiments were performed at SPring-8 with the approval of the Japan Synchrotron Radiation Research Institute (proposal no. 2013A1667).

References

1. Bacabac RG, Smit TH, Van Loon JJ, Doulabi BZ, Helder M, Klein-Nulend J (2006) Bone cell responses to high-frequency vibration stress: does the nucleus oscillate within the cytoplasm? FASEB J 20:858-864
2. Baek K, Barlow A, Allen M, Bloomfield S (2008) Food restriction and simulated microgravity: effects on bone and serum leptin. Journal of Applied Physiology 104:1086-1093
3. Boerckel JD, Kolambkar YM, Stevens HY, Lin AS, Dupont KM, Guldberg RE (2012) Effects of in vivo mechanical loading on large bone defect regeneration. J Orthop Res 30:1067-1075
4. Boerckel JD, Uhrig BA, Willett NJ, Huebsch N, Guldberg RE (2011) Mechanical regulation of vascular growth and tissue regeneration in vivo. Proc Natl Acad Sci U S A 108:E674-680
5. Bosco C, Iacovelli M, Tsarpela O, Cardinale M, Bonifazi M, Tihanyi J, Viru M, De Lorenzo A, Viru A (2000) Hormonal responses to whole-body vibration in men. Eur J Appl Physiol 81:449-454
6. Brotto M, Bonewald L (2015) Bone and muscle: Interactions beyond mechanical. Bone 80:109-114
7. Carano RA, Filvaroff EH (2003) Angiogenesis and bone repair. Drug Discov Today 8:980-989
8. Cheung WH, Sun MH, Zheng YP, Chu WC, Leung AH, Qin L, Wei FY, Leung KS (2012) Stimulated angiogenesis for fracture healing augmented by low-magnitude, high-frequency vibration in a rat model-evaluation of pulsed-wave doppler, 3-D power Doppler ultrasonography and micro-CT microangiography. Ultrasound Med Biol 38:2120-2129
9. Christiansen BA, Silva MJ (2006) The effect of varying magnitudes of whole-body vibration on several skeletal sites in mice. Ann Biomed Eng 34:1149-1156
10. Dan P, Velot É, Decot V, Menu P (2015) The role of mechanical stimuli in the vascular differentiation of mesenchymal stem cells. J Cell Sci 128:2415-2422
11. Doube M, Kłosowski MM, Arganda-Carreras I, Cordelières FP, Dougherty RP, Jackson JS, Schmid B, Hutchinson JR, Shefelbine SJ (2010) BoneJ: Free and extensible bone image analysis in ImageJ. Bone 47:1076-1079
12. Drake CJ, Little CD (1995) Exogenous vascular endothelial growth factor induces malformed and hyperfused vessels during embryonic neovascularization. Proc Natl Acad Sci U S A 92:7657-7661
13. Edwards JH, Reilly GC (2015) Vibration stimuli and the differentiation of musculoskeletal progenitor cells: Review of results in vitro and in vivo. World J Stem Cells 7:568-582
14. Ford NL, Thornton MM, Holdsworth DW (2003) Fundamental image quality limits for microcomputed tomography in small animals. Med Phys 30:2869-2877
15. Garcia P, Pieruschka A, Klein M, Tami A, Histing T, Holstein JH, Scheuer C, Pohlemann T, Menger MD (2012) Temporal and spatial vascularization patterns of unions and nonunions: role of vascular endothelial growth factor and bone morphogenetic proteins. J Bone Joint Surg Am 94:49-58
16. Garman R, Gaudette G, Donahue LR, Rubin C, Judex S (2007) Low-level accelerations applied in the absence of weight bearing can enhance trabecular bone formation. J Orthop Res 25:732-740
17. Garman R, Rubin C, Judex S (2007) Small oscillatory accelerations, independent of matrix deformations, increase osteoblast activity and enhance bone morphology. PLoS One 2:e653
18. Gill TM, Murphy TE, Gahbauer EA, Allore HG (2013) Association of injurious falls with disability outcomes and nursing home admissions in community-living older persons. Am J Epidemiol 178:418-425

19. Groothuis A, Duda G, Wilson C, Thompson M, Hunter M, Simon P, Bail H, van Scherpenzeel K, Kasper G (2010) Mechanical stimulation of the pro-angiogenic capacity of human fracture haematoma: Involvement of VEGF mechano-regulation. Bone 47:438-444
20. Han Y, Cowin SC, Schaffler MB, Weinbaum S (2004) Mechanotransduction and strain amplification in osteocyte cell processes. Proc Natl Acad Sci U S A 101:16689-16694
21. Hausman MR, Schaffler MB, Majeska RJ (2001) Prevention of fracture healing in rats by an inhibitor of angiogenesis. Bone 29:560-564
22. He YX, Zhang G, Pan XH, Liu Z, Zheng LZ, Chan CW, Lee KM, Cao YP, Li G, Wei L, Hung LK, Leung KS, Qin L (2011) Impaired bone healing pattern in mice with ovariectomy-induced osteoporosis: A drill-hole defect model. Bone 48:1388-1400
23. Hung WW, Egol KA, Zuckerman JD, Siu AL (2012) Hip fracture management: tailoring care for the older patient. JAMA 307:2185-2194
24. Hwang SJ, Lublinsky S, Seo YK, Kim IS, Judex S (2009) Extremely small-magnitude accelerations enhance bone regeneration: a preliminary study. Clin Orthop Relat Res 467:1083-1091
25. Judex S, Donahue LR, Rubin C (2002) Genetic predisposition to low bone mass is paralleled by an enhanced sensitivity to signals anabolic to the skeleton. FASEB J 16:1280-1282
26. Kamel HK, Iqbal MA, Mogallapu R, Maas D, Hoffmann RG (2003) Time to ambulation after hip fracture surgery: relation to hospitalization outcomes. J Gerontol A Biol Sci Med Sci 58:1042-1045
27. Komatsu DE, Hadjiargyrou M (2004) Activation of the transcription factor HIF-1 and its target genes, VEGF, HO-1, iNOS, during fracture repair. Bone 34:680-688
28. Kusumbe AP, Ramasamy SK, Adams RH (2014) Coupling of angiogenesis and osteogenesis by a specific vessel subtype in bone. Nature 507:323-328
29. Leung KS, Shi HF, Cheung WH, Qin L, Ng WK, Tam KF, Tang N (2009) Low-magnitude high-frequency vibration accelerates callus formation, mineralization, and fracture healing in rats. J Orthop Res 27:458-465
30. Lin GL, Hankenson KD (2011) Integration of BMP, Wnt, and notch signaling pathways in osteoblast differentiation. J Cell Biochem 112:3491-3501
31. Maes C, Kobayashi T, Selig MK, Torrekens S, Roth SI, Mackem S, Carmeliet G, Kronenberg HM (2010) Osteoblast precursors, but not mature osteoblasts, move into developing and fractured bones along with invading blood vessels. Dev Cell 19:329-344
32. Maes F, Collignon A, Vandermeulen D, Marchal G, Suetens P (1997) Multimodality image registration by maximization of mutual information. Ieee Transactions on Medical Imaging 16:187-198
33. Matsumoto T, Goto D, Sato S (2013) Subtraction micro-computed tomography of angiogenesis and osteogenesis during bone repair using synchrotron radiation with a novel contrast agent. Lab Invest 93:1054-1063
34. Matsumoto T, Itamochi S, Hashimoto Y (2016) Effect of Concurrent Use of Whole-Body Vibration and Parathyroid Hormone on Bone Structure and Material Properties of Ovariectomized Mice. Calcif Tissue Int 98:520-529
35. Matsumoto T, Sato S (2015) Stimulating angiogenesis mitigates the unloading-induced reduction in osteogenesis in early-stage bone repair in rats. Physiol Rep 3
36. Maul TM, Chew DW, Nieponice A, Vorp DA (2011) Mechanical stimuli differentially control stem cell behavior: morphology, proliferation, and differentiation. Biomech Model Mechanobiol 10:939-953
37. McCabe N, Androjna C, Hill E, Globus R, Midura R (2013) Simulated microgravity alters the expression of key genes involved in fracture healing. Acta Astronautica 92:65-72
38. Monfoulet L, Rabier B, Chassande O, Fricain JC (2010) Drilled hole defects in mouse femur as models of intramembranous cortical and cancellous bone regeneration. Calcif Tissue Int 86:72-81

39. Moore D, Leblanc C, Muller R, Crisco J, Ehrlich M (2003) Physiologic weight-bearing increases new vessel formation during distraction osteogenesis: a micro-tomographic imaging study. Journal of Orthopaedic Research 21:489-496
40. Muir J, Kiel DP, Rubin CT (2013) Safety and severity of accelerations delivered from whole body vibration exercise devices to standing adults. J Sci Med Sport 16:526-531
41. Mundy GR, Chen D, Zhao M, Dallas S, Xu C, Harris S (2001) Growth regulatory factors and bone. Rev Endocr Metab Disord 2:105-115
42. Murfee WL, Hammett LA, Evans C, Xie L, Squire M, Rubin C, Judex S, Skalak TC (2005) High-frequency, low-magnitude vibrations suppress the number of blood vessels per muscle fiber in mouse soleus muscle. J Appl Physiol (1985) 98:2376-2380
43. Omar H, Shen G, Jones AS, Zoellner H, Petocz P, Darendeliler MA (2008) Effect of low magnitude and high frequency mechanical stimuli on defects healing in cranial bones. J Oral Maxillofac Surg 66:1104-1111
44. Otsuki T, Takanami Y, Aoi W, Kawai Y, Ichikawa H, Yoshikawa T (2008) Arterial stiffness acutely decreases after whole-body vibration in humans. Acta Physiol (Oxf) 194:189-194
45. Pal N (1996) On minimum cross-entropy thresholding. Pattern Recognition 29:575-580
46. Pasqualini M, Lavet C, Elbadaoui M, Vanden-Bossche A, Laroche N, Gnyubkin V, Vico L (2013) Skeletal site-specific effects of whole body vibration in mature rats: from deleterious to beneficial frequency-dependent effects. Bone 55:69-77
47. Peng H, Wright V, Usas A, Gearhart B, Shen HC, Cummins J, Huard J (2002) Synergistic enhancement of bone formation and healing by stem cell-expressed VEGF and bone morphogenetic protein-4. J Clin Invest 110:751-759
48. Robling AG, Turner CH (2002) Mechanotransduction in bone: genetic effects on mechanosensitivity in mice. Bone 31:562-569
49. Rubin C, Pope M, Fritton JC, Magnusson M, Hansson T, McLeod K (2003) Transmissibility of 15-hertz to 35-hertz vibrations to the human hip and lumbar spine: determining the physiologic feasibility of delivering low-level anabolic mechanical stimuli to skeletal regions at greatest risk of fracture because of osteoporosis. Spine (Phila Pa 1976) 28:2621-2627
50. Schipani E, Maes C, Carmeliet G, Semenza GL (2009) Regulation of osteogenesis-angiogenesis coupling by HIFs and VEGF. J Bone Miner Res 24:1347-1353
51. Stewart JM, Karman C, Montgomery LD, McLeod KJ (2005) Plantar vibration improves leg fluid flow in perimenopausal women. Am J Physiol Regul Integr Comp Physiol 288:R623-629
52. Street J, Bao M, deGuzman L, Bunting S, Peale FV, Ferrara N, Steinmetz H, Hoeffel J, Cleland JL, Daugherty A, van Bruggen N, Redmond HP, Carano RA, Filvaroff EH (2002) Vascular endothelial growth factor stimulates bone repair by promoting angiogenesis and bone turnover. Proc Natl Acad Sci U S A 99:9656-9661
53. Stuermer EK, Komrakova M, Werner C, Wicke M, Kolios L, Sehmisch S, Tezval M, Utesch C, Mangal O, Zimmer S, Dullin C, Stuermer KM (2010) Musculoskeletal response to whole-body vibration during fracture healing in intact and ovariectomized rats. Calcif Tissue Int 87:168-180
54. Szczesny SE, Lee CS, Soslowsky LJ (2010) Remodeling and repair of orthopedic tissue: role of mechanical loading and biologics. Am J Orthop (Belle Mead NJ) 39:525-530
55. Towler DA (2008) The osteogenic-angiogenic interface: novel insights into the biology of bone formation and fracture repair. Curr Osteoporos Rep 6:67-71
56. Usui Y, Zerwekh JE, Vanharanta H, Ashman RB, Mooney V (1989) Different effects of mechanical vibration on bone ingrowth into porous hydroxyapatite and fracture healing in a rabbit model. J Orthop Res 7:559-567
57. Uzer G, Pongkitwitoon S, Ete Chan M, Judex S (2013) Vibration induced osteogenic commitment of mesenchymal stem cells is enhanced by cytoskeletal remodeling but not fluid shear. J Biomech 46:2296-2302

58. Uzer G, Thompson WR, Sen B, Xie Z, Yen SS, Miller S, Bas G, Styner M, Rubin CT, Judex S, Burridge K, Rubin J (2015) Cell Mechanosensitivity to Extremely Low-Magnitude Signals Is Enabled by a LINCed Nucleus. Stem Cells 33:2063-2076
59. Wagatsuma A (2008) Effect of hindlimb unweighting on expression of hypoxia-inducible factor-1alpha vascular endothelial growth factor, angiopoietin, and their receptors in mouse skeletal muscle. Physiol Res 57:613-620
60. Wohl GR, Towler DA, Silva MJ (2009) Stress fracture healing: fatigue loading of the rat ulna induces upregulation in expression of osteogenic and angiogenic genes that mimic the intramembranous portion of fracture repair. Bone 44:320-330
61. Wong LC, Chiu WK, Russ M, Liew S (2012) Review of techniques for monitoring the healing fracture of bones for implementation in an internally fixated pelvis. Med Eng Phys 34:140-152

Figure captions

Fig. 1 (A, B) Radiographs of the drill-hole defect segment of a control mouse tibia on day 12, obtained using synchrotron radiation at 17.9 keV (A) and 18.1 keV (B). The highlighted vasculature in the 18.1-keV image is caused by the K-edge absorption jump of ZrCA. (C, D) Reconstructed images of the defect portion corresponding to A (C) and B (D). Bony callus tissues (dark grey regions) spread in and outward from the drill-hole defect. Light grey regions that are shown in panel D are contrast-enhanced blood vessels. (E, F) Regenerated bone (E) and angiogenic vasculature (F) in a cylindrical region (diameter, 470 μm; height, 110 μm) defined within the cortical defect were obtained by image subtraction between C and D. Bone regions are displayed as extravascular regions with the voxel intensity corresponding to d.HAp > 500 mg/cm^3.

Fig. 2 Three-dimensional images of blood vessels (dark gray) and bone (light gray) in a cylindrical region (diameter, 470 μm; height, 110 μm) at each healing stage. On day 6, formation of irregularly-shaped vessels was observed in both groups with little signs of bone formation. On day 9, a woven-like bone structure was observed in both groups. Blood vessels were more finely distributed in the Vib group compared with shams. On day 12, bone regeneration advanced more in the Vib group than in shams. In contrast, blood vessels occupied a smaller space in the Vib group than in shams.

Fig. 3 Vessel thickness histogram on days 6, 9, and 12, indicating the vessel number density (V.N) for seven vessel thickness ranges. Capillary-sized vessels with a thickness of < 8 μm on day 9 showed a trend toward a higher V.N in the Vib group than in shams (P = 0.065). For the other vessel thicknesses, V.N in the Vib group was smaller than or similar to that in shams from days 6 to 12. $^{*}P < 0.05$, $^{**}P < 0.01$ vs. sham.

Fig. 4 Relative distribution of bone volume versus density of hydroxyapatite (d.HAp) within the defect region on days 9 and 12. The relative bone volume at each d.HAp value (bin width: 6.54 mg/cm^3) is expressed as a percentage of the total volume of voxels with d.Hap > 500 mg/cm^3. The distribution on day 12 peaked at a higher d.HAp in the Vib group than in shams (885 ± 23 vs. 842 ± 46 mg/cm^3, $P < 0.05$).

Fig. 5 Strain signals from a longitudinal strain gauge that was bonded on the tibial diaphyseal surface (broken lines). Signals were obtained from the same mouse standing on the vibration platform in the operated state (A) and in the non-operated state (B). Processing with a 28–32-Hz band-pass filter highlights the LIWBV-associated sine-wave oscillation (solid lines). In this recording, the peak-to-peak signal amplitude in the 28–32-Hz band increases more than four-fold by LIWBV loading.

Figure 1

Click here to download Figure Fig_1.tif

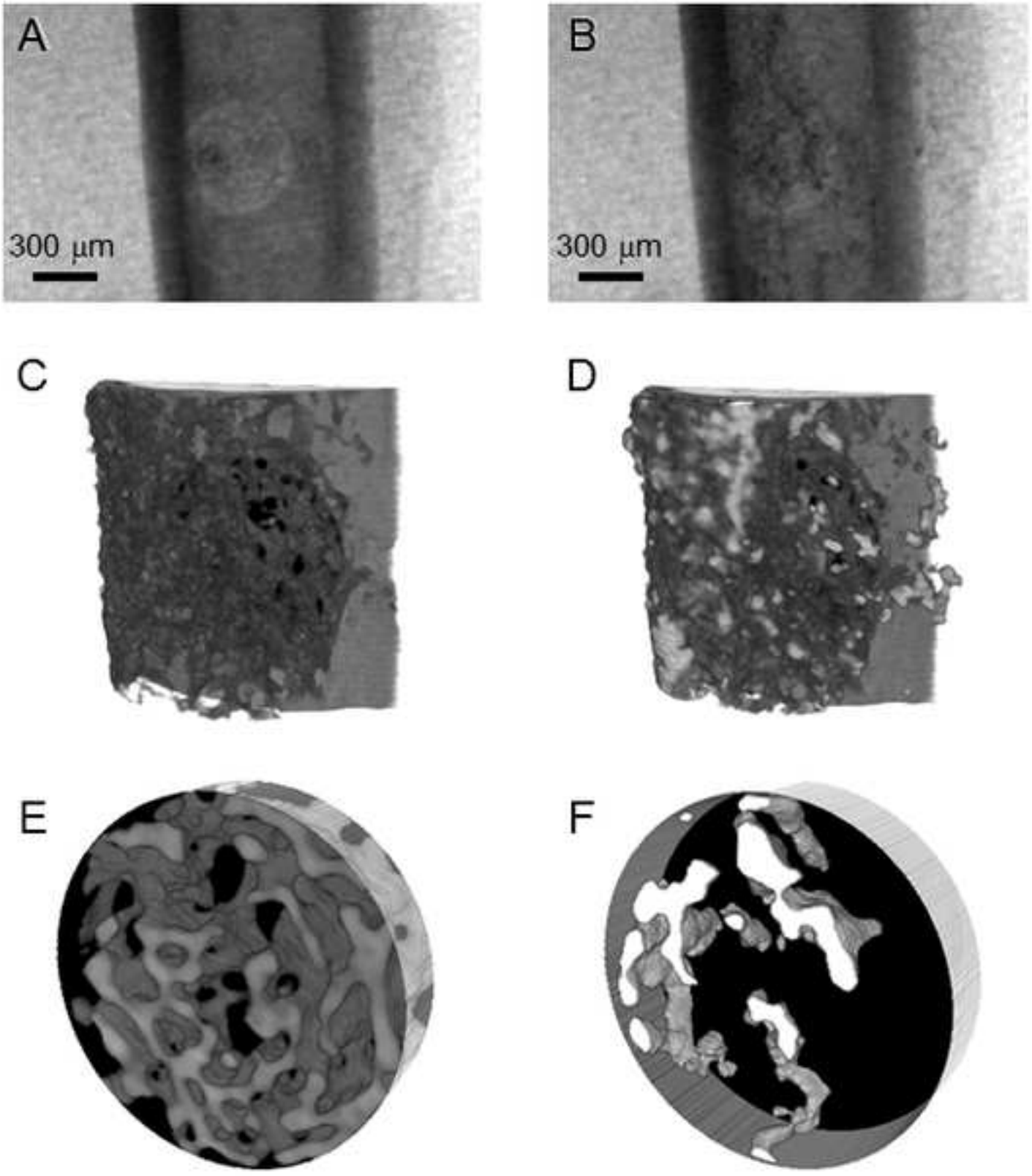

Figure 2

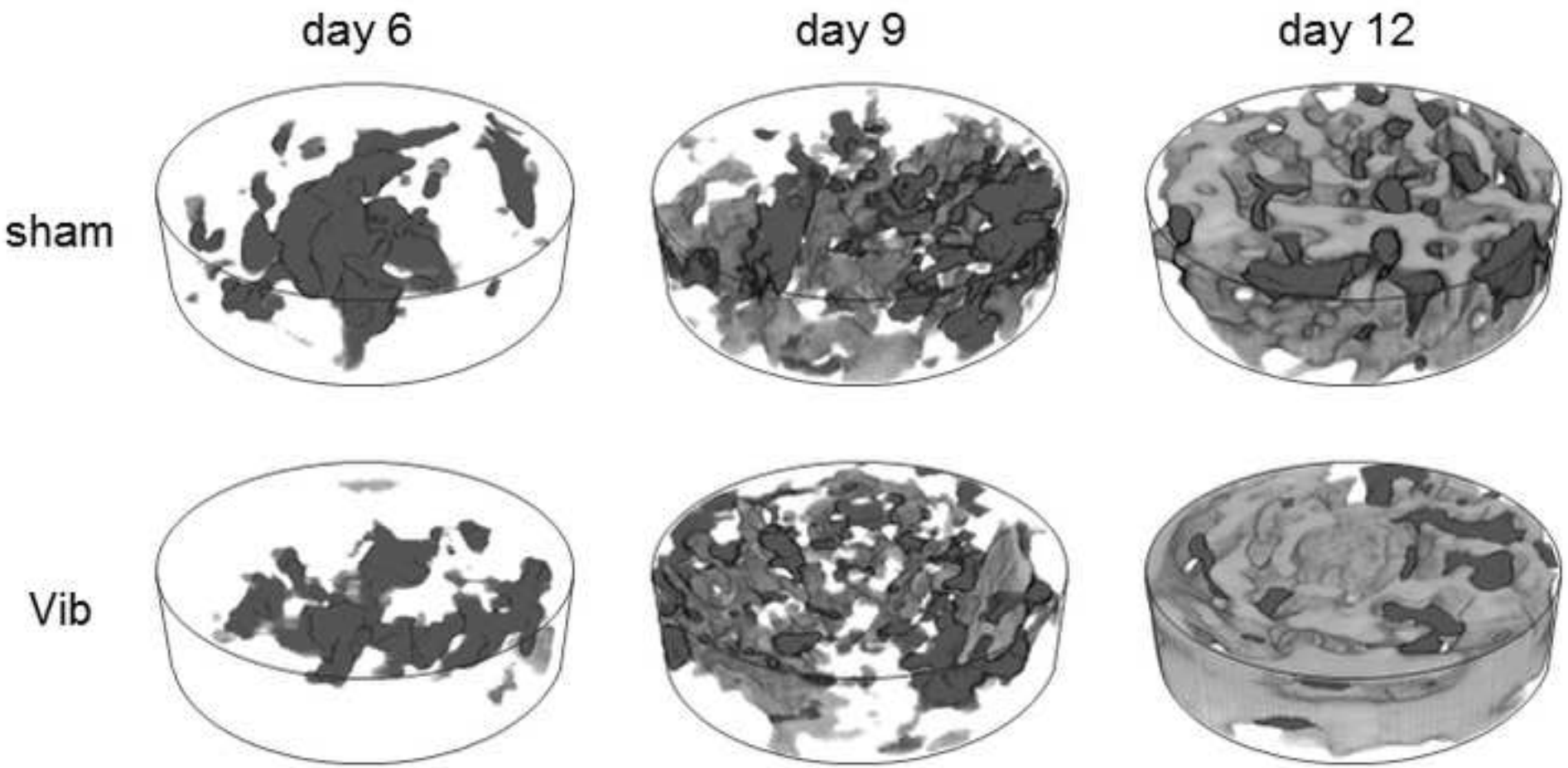

Figure 3

Click here to download Figure Fig_3.tif

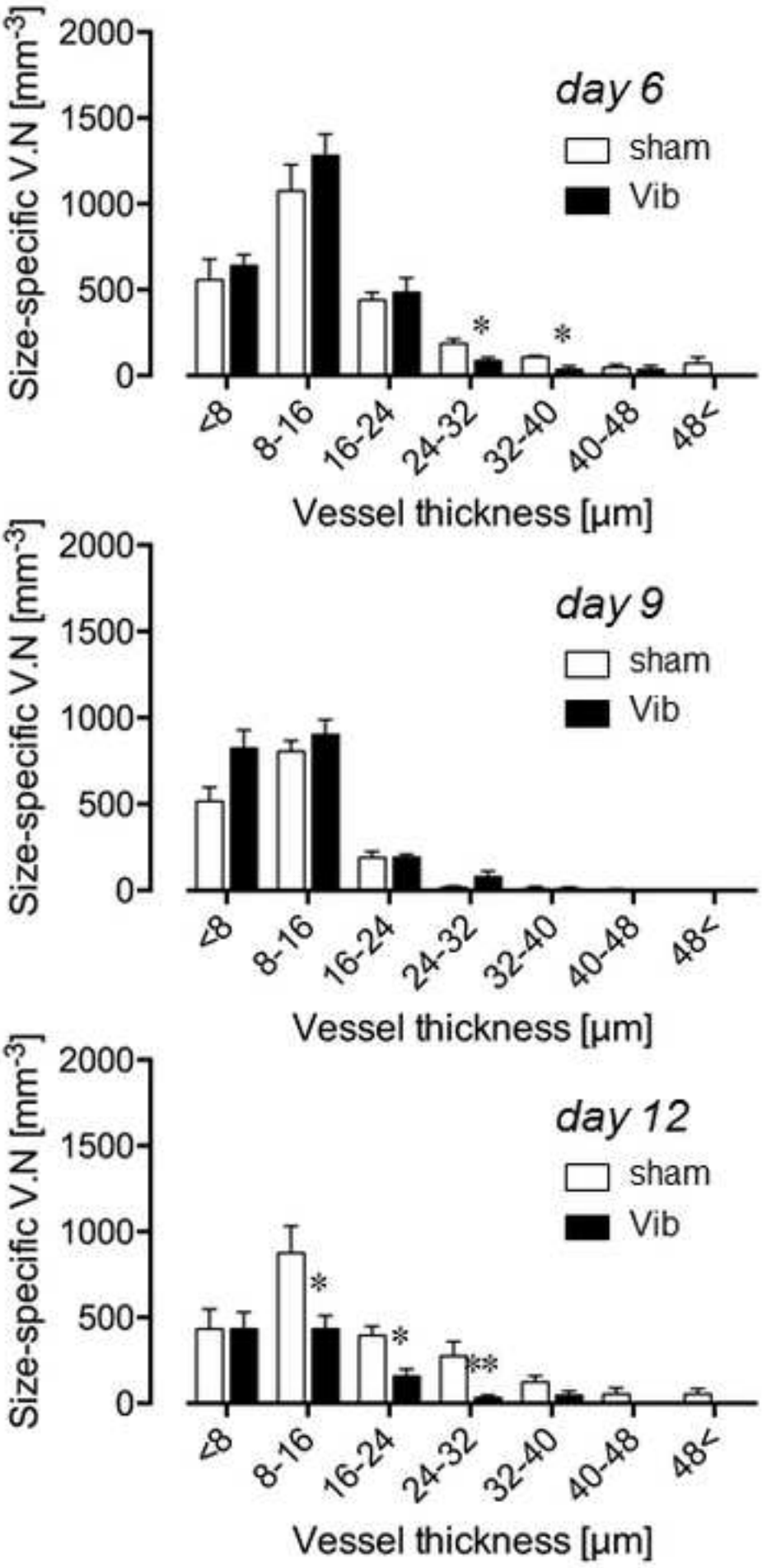

Figure 4

Click here to download Figure Fig_4.tif

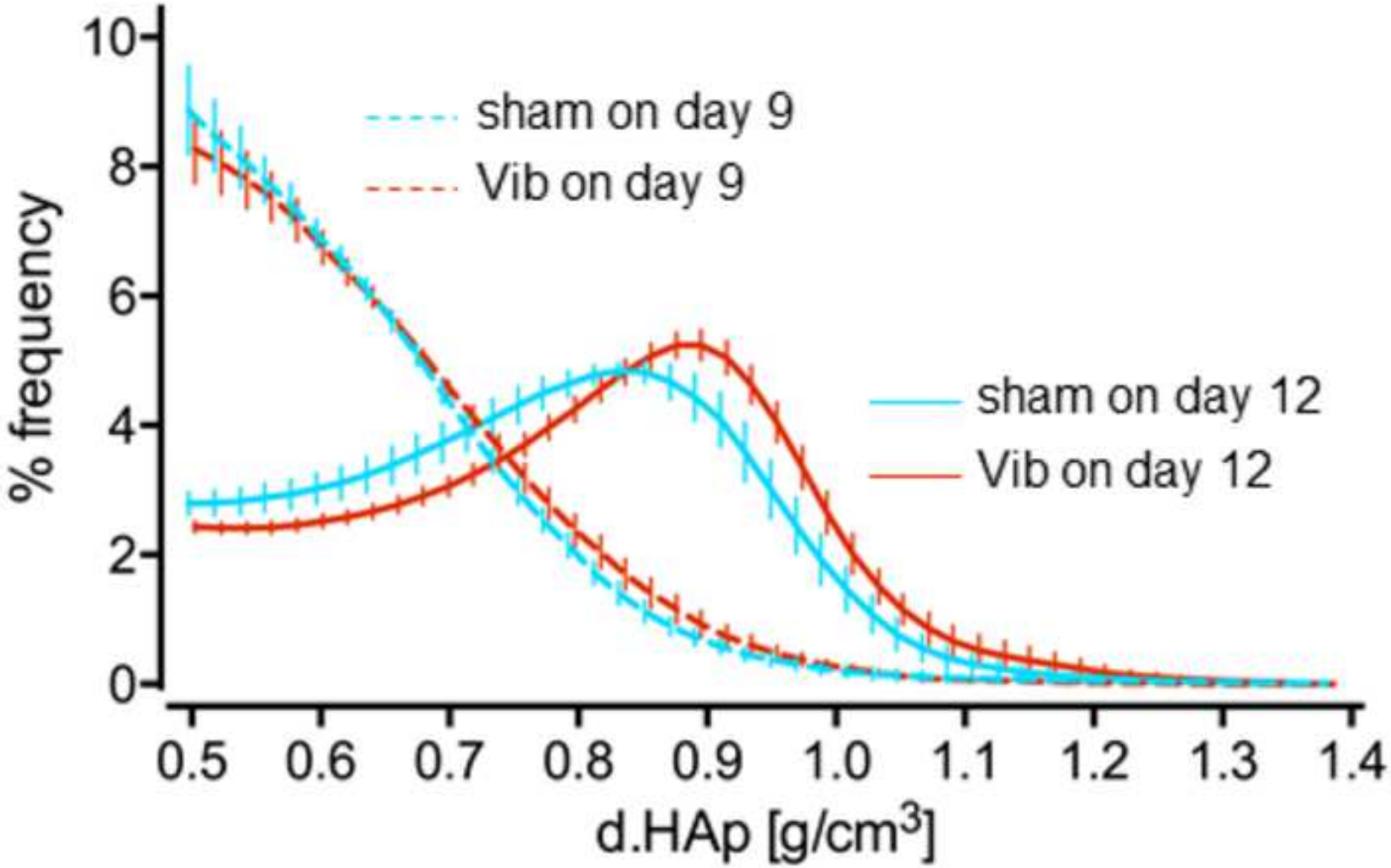

Figure 5

Click here to download Figure Fig_5.tif

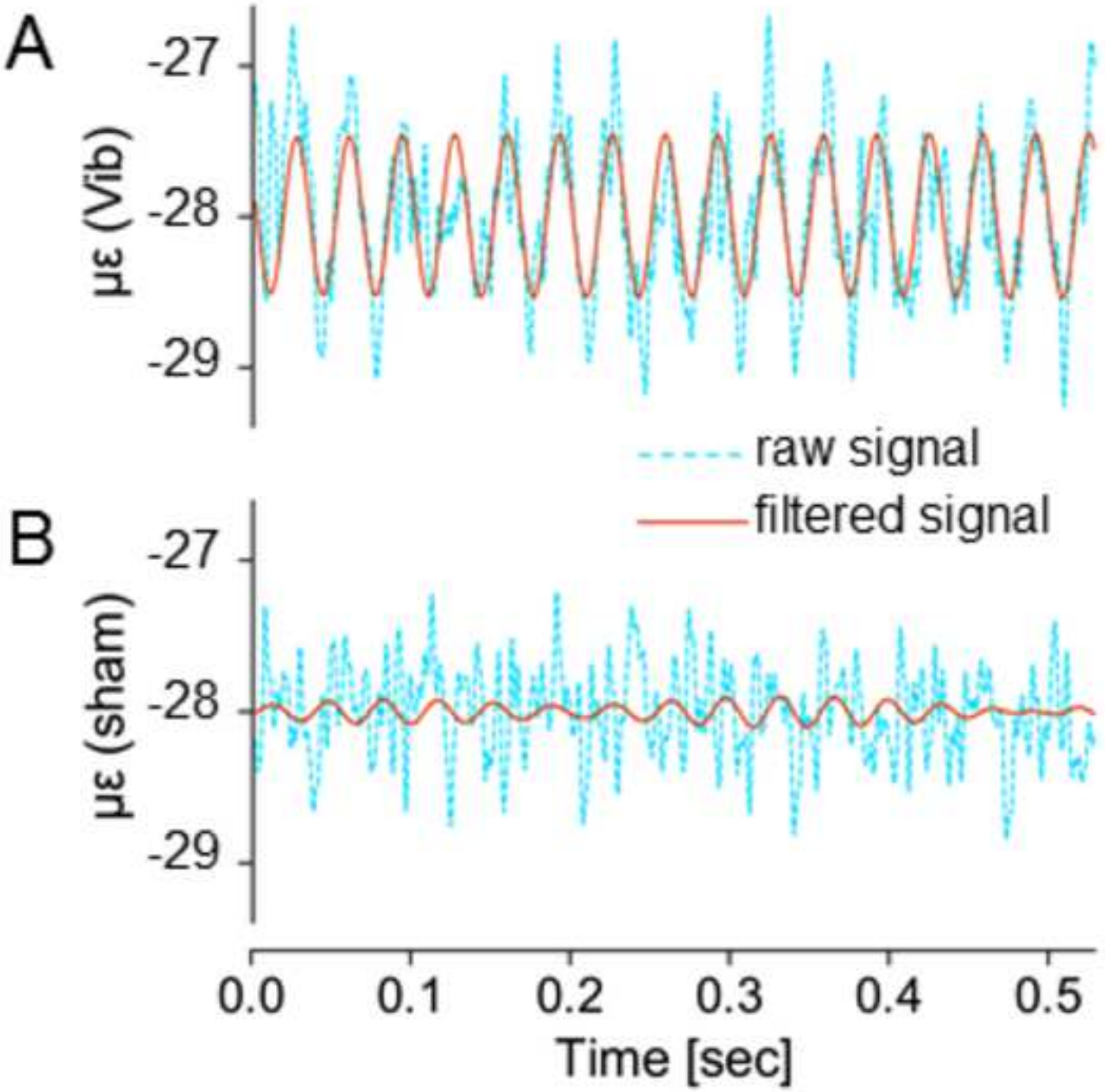

Table 1 Bone and vascular structural indices

	day 6		day 9		day 12	
	sham	Vib	sham	Vib	sham	Vib
B.Vf (%)	n/a	n/a	17.2±2.2	18.8±1.2	44.0±1.4^{bb}	54.2±1.4$^{**, bb}$
B.Th (μm)	n/a	n/a	20.1±0.6	20.1±0.7	29.3±0.9^{bb}	34.3±1.5$^{**, bb}$
B.Sep (μm)	n/a	n/a	60.3±3.6	60.6±2.7	44.5±2.4^{bb}	39.4±2.2$^{*, bb}$
V.Vf (%)	21.0±4.4	12.0±2.4	3.9±0.7^{aa}	4.4±0.6^{a}	12.0±2.1^{b}	3.8±0.8**
V.Th (μm)	15.5±1.2	12.7±0.4*	11.0±0.8^{a}	10.7±0.7	17.1±1.7^{b}	11.6±1.2
V.N (mm^{-3})	2558±249	2573±255	1567±127^{a}	2032±61*	2225±238^{b}	1111±188$^{**, b}$

B.Vf bone volume fraction, *B.Th* bone thickness, *B.Sep* bone spacing, *V.Vf* vascular volume fraction, *V.Th* vessel thickness, *V.N* the number density of node-to-node or node-to-free-end vessel segments. $^{*}P < 0.05$, $^{**}P < 0.01$ vs. sham; $^{a}P < 0.05$, $^{aa}P < 0.01$ vs. day 6; $^{b}P < 0.05$, $^{bb}P < 0.01$ vs. day 9.